Three-dimensional pore networks and transport properties of a shale gas formation determined from focused ion beam serial imaging

Thomas A. Dewers*

Geomechanics Department,
Sandia National Laboratories,
Albuquerque, New Mexico, 87185, USA
E-mail: tdewers@sandia.gov
*Corresponding author

Jason Heath

Geophysics and Atmospheric Sciences Department,
Sandia National Laboratories,
Albuquerque, New Mexico, 87185, USA
E-mail: jeheath@sandia.gov

Russ Ewy and Luca Duranti

Chevron Energy Technology Company,
San Ramon, California, 94583, USA
E-mail: RussEwy@chevron.com
E-mail: lduranti@chevron.com

Abstract: Three-dimensional pore network reconstructions of mudstone properties are made using dual focused ion beam-scanning electron microscopy (FIB-SEM). Samples of Jurassic Haynesville Formation mudstone are examined with FIB-SEM and image analysis to determine pore properties, topology, and tortuosity. Resolvable pore morphologies (>~10 nm) include large slit-like pores between clay aggregates and smaller pores in strain shadows surrounding larger clastic grains. Mercury injection capillary pressure (MICP) data suggest a dominant 1–10 nm or less size of pores barely resolvable by FIB-SEM imaging. Computational fluid dynamics modelling is used to calculate single phase permeability of the larger pore networks on the order of a few nanodarcys (which compare favourably with core-scale permeability tests). This suggests a pore hierarchy wherein permeability may be limited by connected networks of inter-aggregate pores larger than about 20 nm, while MICP results reflect smaller connected networks of pores residing in the clay matrix. [Received: May 12, 2011; Accepted: September 14, 2011]

Keywords: shale gas; Haynesville formation; pore networks; focused ion beam; FIB.

Reference to this paper should be made as follows: Dewers, T.A., Heath, J., Ewy, R. and Duranti, L. (2012) 'Three-dimensional pore networks and transport properties of a shale gas formation determined from focused ion beam serial imaging', *Int. J. Oil, Gas and Coal Technology*, Vol. 5, Nos. 2/3, pp.229–248.

Biographical notes: Thomas A. Dewers is a principal member of the technical staff in the Geomechanics Department at Sandia National Laboratories in Albuquerque, New Mexico. He has over 21 years experience in industry, academia, and government relating to work in the geosciences, and holds a PhD in Geology. His current research interests include nano-to-reservoir scale inquiries into rock mechanics, multiphase flow and reactive transport.

Jason Heath is a senior member of the technical staff of the Geophysics and Atmospheric Sciences Department, Sandia National Laboratories, Albuquerque, New Mexico. He has a PhD and MS in Hydrology and Geology, respectively. His research focuses on efficiently estimating well injectivity for large-scale CO_2 storage projects, CO_2-water-rock interactions, and caprock sealing behaviour.

Russ Ewy is a Research Consultant with Chevron Energy Technology Co., where he performs research and technical service in the areas of reservoir and wellbore geomechanics, and leads multidisciplinary research on shales. He holds a BS and MEng in Mineral Engineering and a PhD in Rock Mechanics, all from the U. of California at Berkeley. He has served on the board and the executive committee of the American Rock Mechanics Association, and currently serves as a Review Chair for the *Society of Petroleum Engineers Journal*.

Luca Duranti is a Senior Research Geophysicist at Chevron Energy Technology Company, in San Ramon, California. He has 15 years of industry experience in industry and academia, primarily in research but including operational aspects, and holds a PhD in Geophysics from Colorado School of Mines. His current research interests are in experimental and theoretical poroelasticity, spanning across the wide spectrum of granular media, their interaction with fluids in depositional as well as production environments, and their detection in the active and passive seismic signal.

1 Introduction

Shale gas plays around the world have generated interest in the variety and structure of pore networks in mudstones. Typically, three dimensional imaging of these tiny pore systems have been inaccessible via microCT and/or optical methods due to resolution issues. SEM and TEM imaging methods can resolve useful two-dimensional information for mudstone pore sizes down to nanometre (nm) sizes (Desbois et al., 2008, 2009; Loucks et al., 2009). In conjunction with successive FIB milling of nanometre-scale surfaces (Yao, 2007), image stacks are obtained that can be used to reconstruct three dimensional digital pore and mineral structures (Heath et al., 2011). These are akin to microCT and laser scanning confocal image sets for larger pore-sized sandstones. Together, dual FIB-SEM methods can be a powerful tool in understanding pore types (Holzer et al., 2004; Loucks et al., 2009; De Winter et al., 2009), pore networks (Heath et al., 2011) and matrix flow properties (Tomutsa et al., 2007) in shale gas mudstones and other rock types.

In this paper, samples of mudstone from the Upper Jurassic Haynesville Formation (Tolson et al., 1983), a prominent new shale gas play underlying much of the US Gulf

Coast, are examined using FIB-SEM methods. The Haynesville Formation represents an Upper Jurassic post-rift transgressive deposit and encompasses an array of anhydrites, limestones, mudstones and eolian, fluvial, and alluvial sandstones (Mancini et al., 1997). It lies beneath the Smackover Formation ramp deposit carbonates and above the Cotton Valley Group fluvial-deltaic sands (Dobson and Buffler, 1997).

Image stacks with 7.14 nm pixel size are obtained for Haynesville mudstone volumes cubic microns in size. Pore properties including porosity, pore body volume and throat size distributions, pore connectivity, and tortuosity are extracted from the reconstructed three-dimensional digital pore structures using image analysis techniques and software. FIB-SEM- derived pore throat distributions are compared to those estimated from mercury porosimetry (MP), the latter emphasising the smaller pores in the distribution. Single phase permeabilities are estimated from computational fluid dynamics (CFDs) modelling to be in the range of 2 to 12 nanodarcies (nD), which are similar to values obtained from core plug measurements (5 to 50 nD). These digital pore reconstructions and modelling can aid in interpretation of core-scale geomechanical and single and multiphase flow properties.

Figure 1 SEM image of 25 micron-wide trench in Haynesville formation mudstone sample, cut using a Ga ion beam

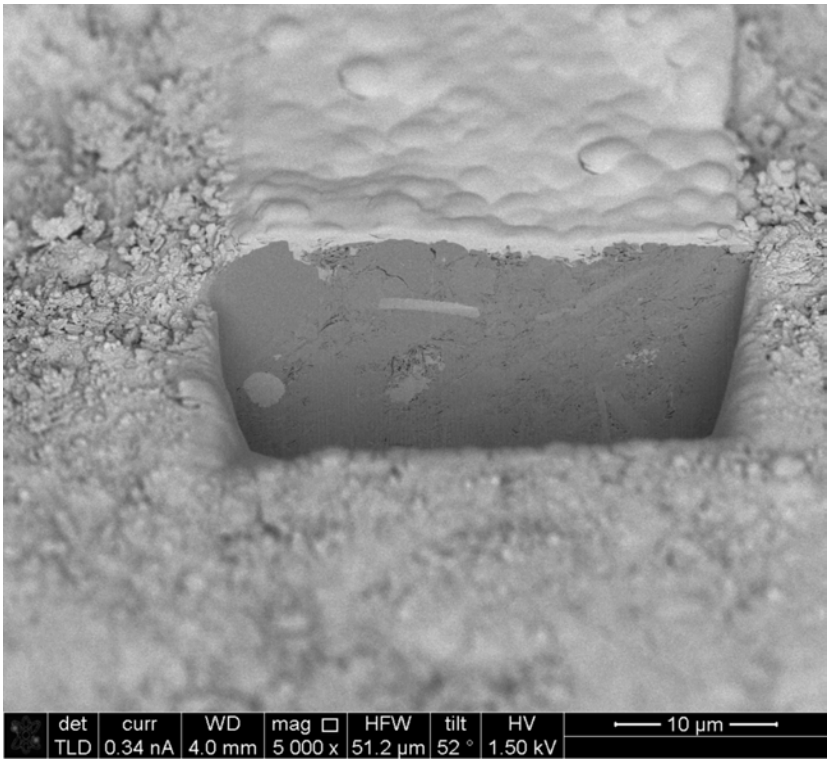

Notes: The light grey material on top of the mudstone is a platinum coating, used to minimise non-planar 'curtaining' during ion beam sectioning. Imaging is done in a 'pseudo-back scatter' mode, so that grey levels on the flat mudstone surface vary with mean atomic number and thus correlate with different mineral phases.

Figure 2 Four SEM photomicrographs of Haynesville fm. mudstone FIB slices, imaged at 7.14 nm pixel resolution

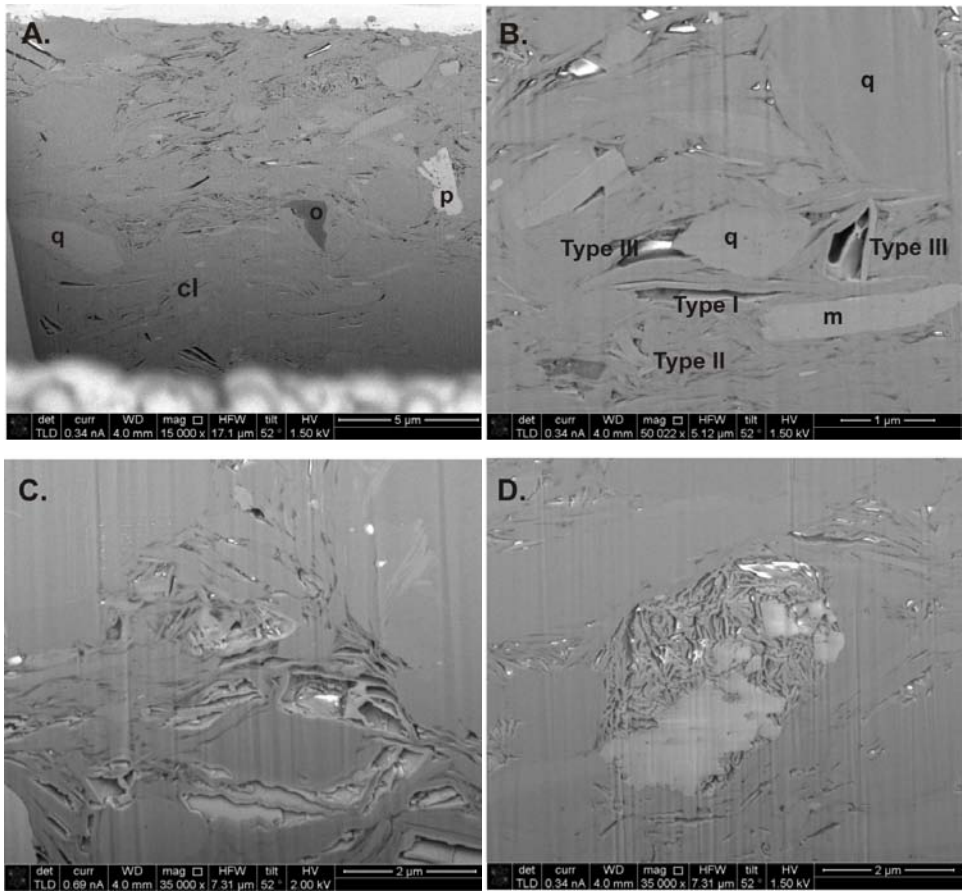

Notes: The ‘up’ direction in all photos is the depositionalyounging direction. White spots in all images are due to charging by secondary electrons and usually occur at edges or interiors of pores.

(a) Close-up of FIB trench (note blurry platinum coating in foreground at bottom). Mineral (quartz, q, pyrite, p, and clay matrix, cl) and organic (o) phases are discernable by differing grey levels (due to variation in mean atomic number).

(b) Types of pores, following the classification scheme of Heath et al. (2011) after Desbois et al. (2009). Type I pores (a prime example is located just above the label) are slit shaped and oriented perpendicular to depositional direction. Type II pores (in the vicinity of the label) are crescent-shaped pores residing in clay matrix. Type III pores (examples are located to the right of the left-most label and to the left of the right-most label) are associated with the compaction shadows of larger clastic (commonly quartz, q) grains. Light grey rectangular grain is detrital mica (m).

(c) Micron-sized Type II and Type III pores in clay fabric.

(d) Open pore fabric of possible diagenetic clay (chlorite?) partially filled with what islikely calcite (?, light grey) surrounded by tighter clay matrix.

2 Methods

2.1 FIB-SEM imaging

One-inch core plugs of Hayneville Formation mudstones were provided by Chevron. Pieces of these with known orientation were gold-palladium coated and a portion coated with silver dag to minimise sample charging. Serial sectioning and imaging was done using an FEI Helios 600 NanolabDualBeam™ instrument and SliceandView™ software. A layer of platinum was deposited on top of the portion of sample to be sliced to minimise the vertical striations or curtaining that often plague ion milling (Figure 1). Ion milling was performed using a 30 kV Ga ion beam with current of 2.8 nA. Vertical slices 15 nm thick was obtained by successive ion milling. SEM imaging of slices 10's of square microns in size was done in backscattered mode with a through-the-lense detector, 1 kV voltage and 1.4 nA current. This was done to best enable discernment of pores, minerals, and organic matter, the latter two due to differences in mean atomic number (Figure 2). Five sampling sites were selected based on visual inspection for representativeness of the dominant mudstone microfacies. The data set presented here was selected for further analysis based on quality of images and large size of the image stack that was obtained. The volume of the final data set examined is a result of imaging constraints by the FIB/SEM Helios Nanolab.

2.2 Image processing and analysis

The resulting image stacks required a number of image processing steps in order to obtain three dimensional reconstructions. We used the ImageJ software (version 1.44p; Rasband, 2010; Ferreira and Rasband, 2010) to align and crop the image stacks. The *ImageJ*™ plugin *TransformJ*™ (Meijering, 2010) was used to interpolate between the image stacks to obtain a final cubic voxel size of 7.14 nm. Thresholding or segmentation of the image stack proved challenging due to the extensive charging of certain pore lining phases and pore walls [Figure 2; Figure 3(a)]. To circumvent this, we used a two-step segmentation where dark pores (observed in Figure 2 images) were first thresholded, and then combined with a stack segmented for the bright white charging locations, which always coincided with pores [Figure 3(b)]. The resulting series of two dimensional images [e.g., Figure 3(c)] were assembled into a three dimensional stack and rendered as a 3D surface using *ScanIP*™ software (Figure 4). Dimensions of the volume were 930 × 434 × 1,036 pixels, and with a pixel size of 7.14 nm, this results in a total imaged size of 6.6 (in x) by 3.1 (in y) and 7.1 (in z) microns, or a volume of 152.2 cubic microns.

The final segmented images were input into the *3DMA-Rock* software (Lindquist, 1999; Lindquist and Venkatarangan, 1999; Lindquist et al., 2005) which was used to calculate the medial axis (the middle axis of voxels running through pores, resulting in a 3D skeleton representation of the network of connected pores; Figure 5(a) and Figure 5(b). Medial axes also were used to determine cross-linked pathways (i.e., topology) through the pore networks and calculation of tortuosity (Figure 6). Once the medial axis was constructed, 3DMA-Rock algorithms were then used to define pore throats from pore bodies, based on the 'wedge finding' algorithm (Shin et al., 2005).

Figure 3 Sequence of images used in three dimensional pore reconstructions (see online version for colours)

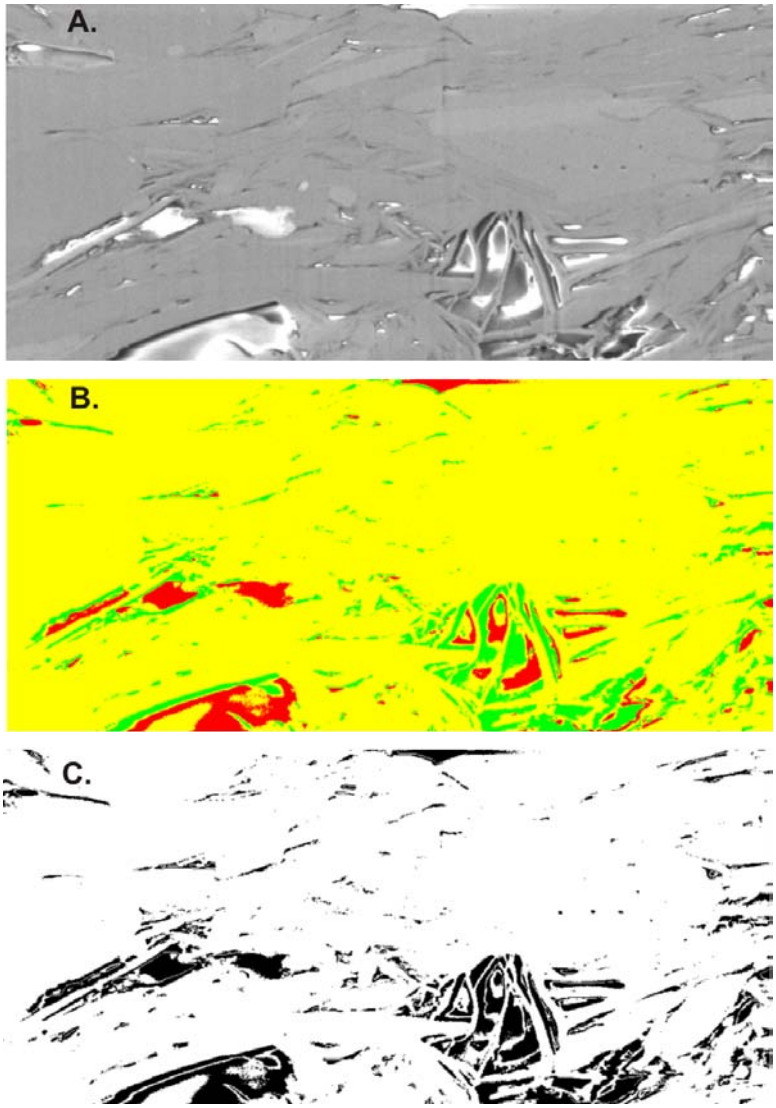

Notes: (a) Original image slice showing small dark pores and larger pores with charging (bright white spots), as well lighter grey variations corresponding to mineral phases.

(b) Combined segmented images into mineral (yellow), green (pores) and charging regions (red). Segmenting was performed using the Otsu thresholding algorithm (Rasband, 2010).

(c) Final data set segmented into pore (black) and solid (white), formed by combining the two pore grey levels in (b).

Figure 4 Visualisation of resolved pores for three dimensional portion of Haynesville formation mudstone (see online version for colours)

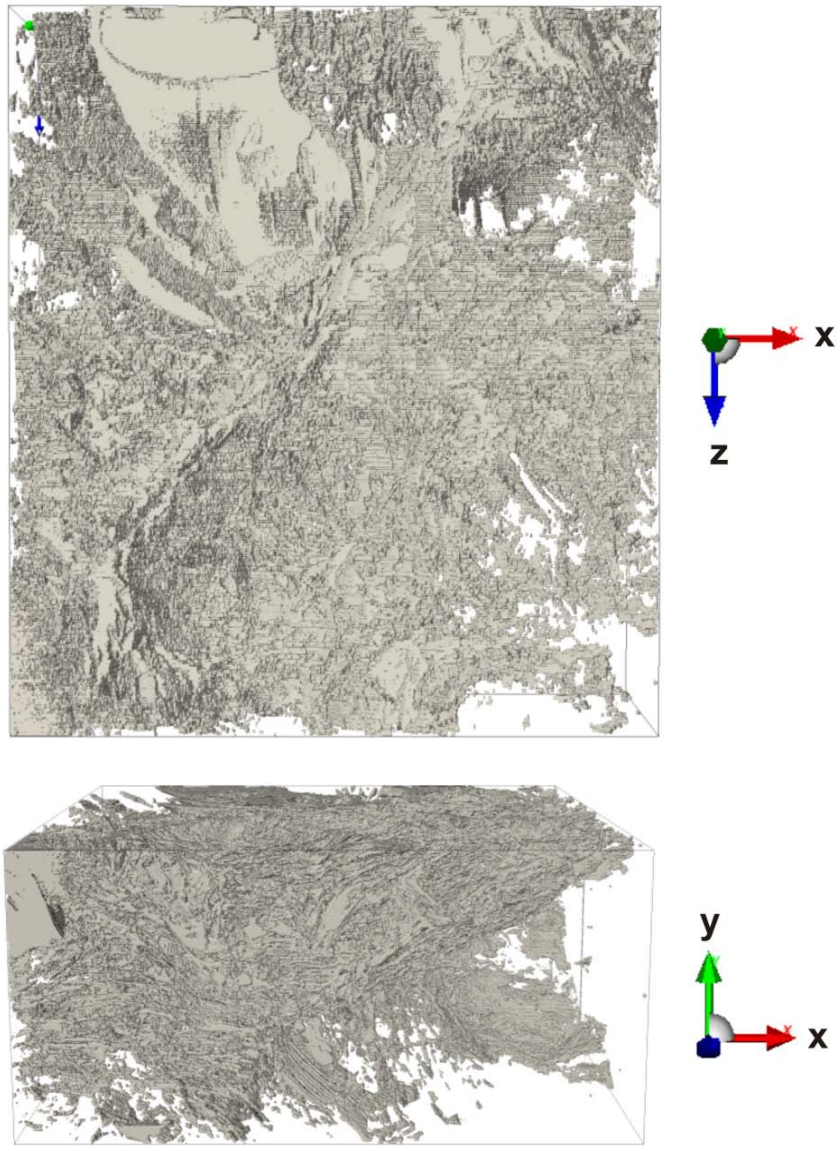

Notes: Pores are shown as grey solid masses. Large open regions correspond to locations of large quartz grains. Note what appears to be a large pore network 'rib' running from lower left to upper right in the xz (top) view. Dimensions are 930 × 434 × 1,036 pixels, and with a pixel size of 7.14 nm, this results in a total imaged size of 6.6 (in x) by 3.1 (in y) and 7.1 (in z) microns, or a volume of 152.2 cubic microns.

Figure 5 Medial axes and joint histogram of pore properties for Haynesville formation mudstone sample (see online version for colours)

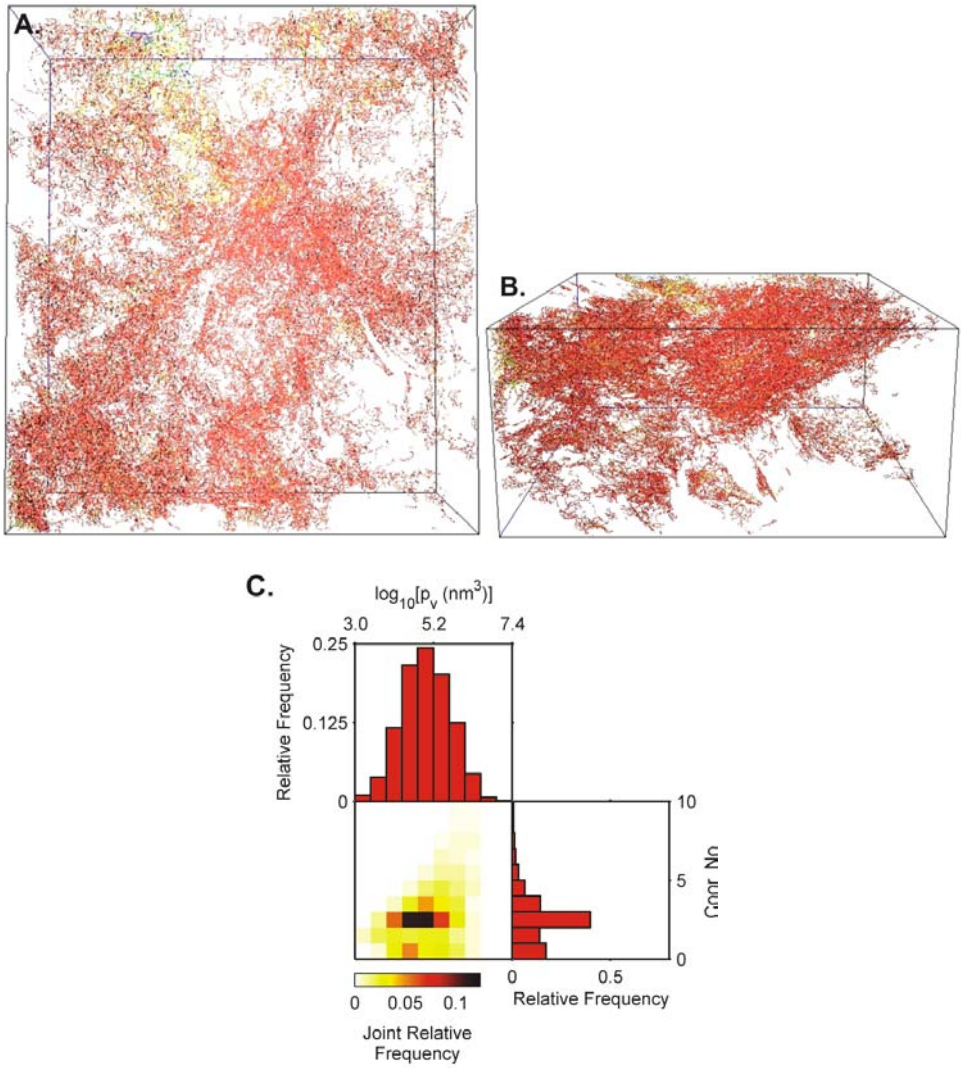

Notes: (a) and (b) Map and oblique views of pore network medial axes (same views as Figure 4), obtained by connecting medial axis (MA) voxels into a 3D skeleton of the porous framework. The pore network 'rib' observed in Figure 4(a) is seen as a higher density of MA voxels. Areas of little or no density of MA voxels correspond to large clastic grains, likely quartz.
(c) Joint and marginal relative frequency histograms of pore body volume and coordination number (Coor. no.). The maximum relative frequency of the joint histogram is 0.12 (black). The marginal histogram for coordination number is such that the bottom horizontal bin is for pore bodies of zero coordination number. The second bin is for those with coordination number of 1, and so on in integer values up to a coordination number of 10. This shows that the mean log10 (pore volume) of ~4.5 are pores with the most frequent coordination number of 2.

Figure 6 Shortest connected pathways and tortuosity of Haynesville formation sample (see online version for colours)

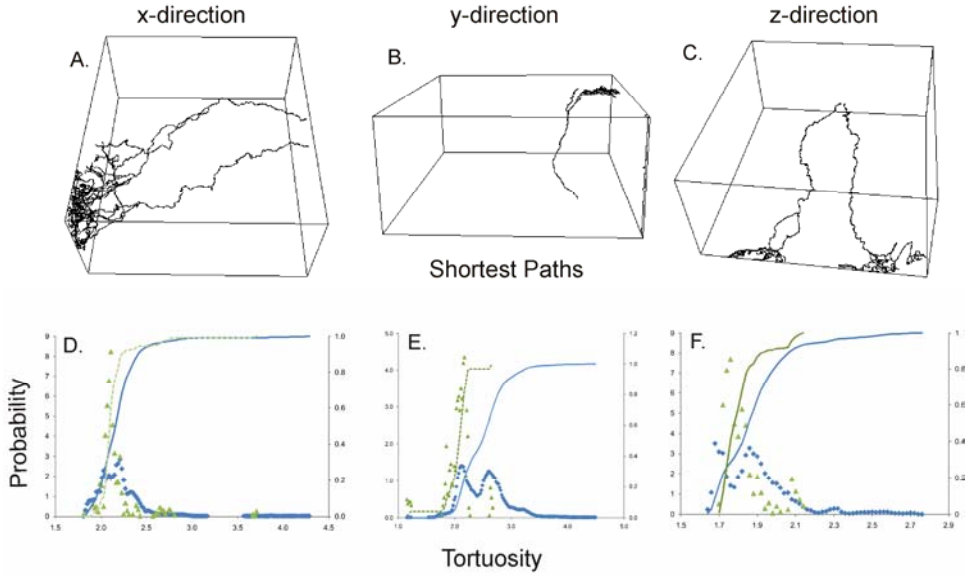

Notes: (a) through (c). Shortest connected pathways through the reconstructed mudstone volume in the x-, y-, and z-direction respectively. The x-pathways were chosen from left to right as shown, y-pathways were chosen from top to bottom as shown, and z-pathways were chosen from front to back as shown. (d) through (f). Probability distributions (constructed from frequency histograms) of tortuosity through the pore network in the x-, y-, and z-directions respectively, defined as actual voxel x- y- or z-path length divided by the x-, y-, or z-dimension. Green symbols show actual values for the shortest path lengths shown in (a)–(c), while blue symbols are all calculated paths. Blue and green lines show the cumulative probability distribution for all and shortest paths respectively.

ScanIP™ algorithms were applied to the segmented image stack to visualise connected pore networks by a 'floodfill' algorithm. Two large domains of connected pores (Figure 7) were then selected and used to generate tetrahedral finite element meshes with *ScanIP*™. Mesh size was selected to achieve at least si elements across the smaller pore throats.

2.3 CFD modelling

CFDs modelling of incompressible Navier-Stokes flow were done using *COMSOL Multiphysics*™ and the *ScanIP*™-derived finite element meshes. No-slip boundary conditions were applied to pore walls, and constant pressure was applied to inlet and outlet portions of the pore network so as to apply a small pressure gradient (0.1 Pa/m) across the z-direction, assuming a fluid (water) density and viscosity of 1,000 kg/m^3 and 0.001 Pa-s respectively. Permeability of the pore networks estimated from the applied pressure gradient (outlet pressure minus inlet pressure divided by Euclidian distance between them, L), inlet surface area A, fluid viscosity μ, and modelled flux Q using Darcy's Law expressed as

$$Q = \frac{Ak}{\mu}\left(\frac{Poutlet - Pinlet}{L}\right) \tag{1}$$

and solving for k. This assumes that the pore networks contain a sufficient number of pores to be a representative elementary volume (REV), so that the continuum concept of Darcy's Law is applicable. A detailed examination of what constitutes a REV in mudstones is beyond the scope of what we attempt here, but FIB/SEM methods as examined here may provide the necessary resolution to address this question.

Figure 7 Examples of connected networks of Haynesville formation pores (see online version for colours)

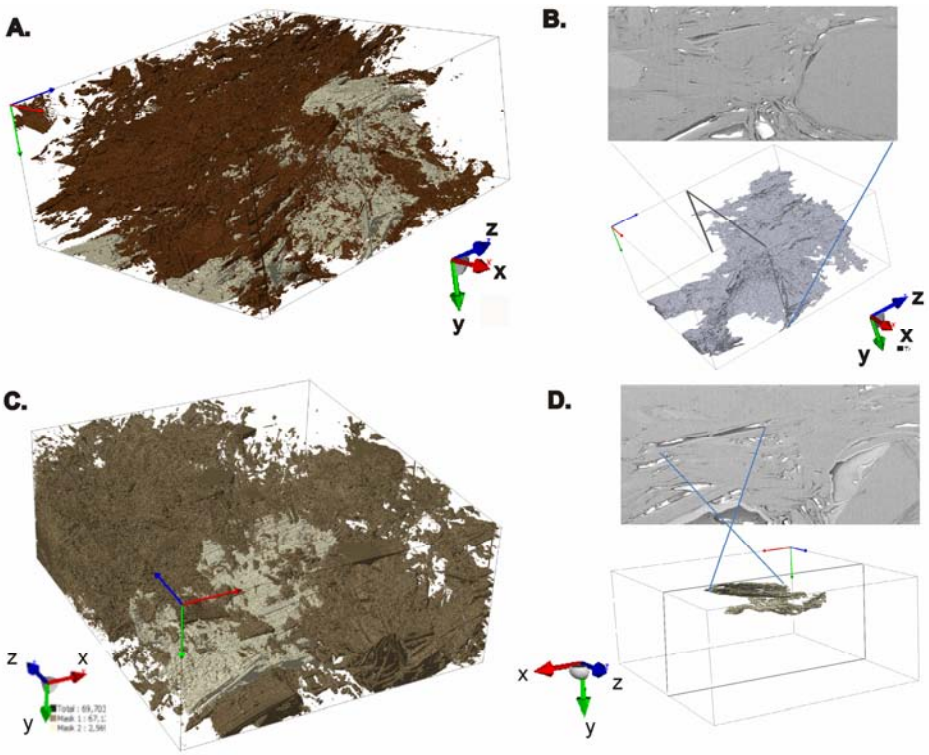

Notes: (a) View of large swath of connected pores (light grey), which are not connected to remaining pores in the sampled volume (dark brown), constructed using a flood-fill algorithm.

(b) 2D FIB-SEM image and 3D view with cross section corresponding to this image. Note the large quartz grain in the right of the image. This pore network largely is adjacent to, and in the 'strain-shadow' of, the large quartz grain.

(c) Connected network of 'slit' pores, shown in light grey, which is disconnected from remaining pores as determined using flood-fill algorithm.

(d) 2D FIB-SEM image and 3D view with cross section of slit pore network, consisting of two large crack-like pores connected by a narrow throat. Note what appears to be a faceted quartz grain in the lower right portion of the photomicrograph.

2.4 Mercury porosimetry

Mercury injection porosimetry (MIP) was performed on two plugs of proximal locality to the FIB-SEM samples investigated here. The plugs were oven dried for 24 hours at 50°C, exposed to a vacuum, and then mercury was injected with step-wise pressure increase in an omni-directional fashion. Raw volume-pressure data were subjected to a conformance correction (Almon et al., 2008; Sigal, 2009), which sets the upper boundary for MIP pore statistics.

2.5 Pulse decay permeability of cores

Permeability of mudstone samples were measured on 1 inch (25 mm) right cylindrical core plugs with helium using a variation of the pulse decay technique as described by Jones (1997). This involves creating a pressure difference between a tightly jacketed sample and upstream and downstream reservoirs and collecting pressure pulse decay data from upstream reservoir and downstream reservoirs. Core plugs were taken from the same core but from a slightly different depth as the samples used for FIB/SEM analysis. Measurements were done on core plugs in an as-received (nominally dry) condition, so that the plugs probably contained water within the smallest pores.

3 Results

3.1 Haynesville formation mudstone composition and core-plug petrophysical properties

X-ray diffraction of core samples near those used for imaging show a typical mudstone mineralogical suite consisting of between an estimated 13%–15% (by weight) quartz, 8%–12% plagioclase, 15%–21% carbonate (mostly calcite), 10%–12% chlorite and 33%–40% dioctahedral 2:1 layer clay which includes mixed layer illite-smectite, discrete illite, smectite and detrital micas (determined using methods outlined by Srodon et al., 2001). Together with the ~5% kerogen (from total organic carbon measurements), this constitutes 43 to 52% by weight of clay and 48%–57% non-clay. RockEval measurements of total organic content for two samples are ~3.4% by weight.

Porosity estimations vary by method of measurement. MICP, which probably underestimates total porosity estimates for two measured samples range between 3.7 and 4.7%. Porosity (estimated from weight and volume of dried plug) -effective stress measurements were performed on a dried plug and show a linear decrease of porosity with effective stress (porosity values at 14 MPa, 27 MPa, and 41 MPa were 12%, 11%, and 9% respectively). Extrapolation this linear relationship back to zero effective stress gives a porosity value of 12.8%. Gas permeability from three samples ranged from 20 to 55 nanodarcy (2.0 to 5.4 $\times$ 10^{-20} m^2) at 2,000 psi (13.8 MPa) confining pressure, and dropped to ~5 nanodarcy (~ 5 $\times$ 10^{-21} m^2) for all three samples at 6,000 psi (41.3 MPa).

3.2 Imaged mudstone pore types

The four photomicrographs in Figure 2 display some of the variety of mineral and pore types observed by FIB-SEM in the Haynesville Formation mudstone samples. Figure 2(a) shows quartz (q) grains suspended in a matrix of clay minerals (cl). Kerogen appears in rare patches [labelled 'o' in Figure 2(a)], and unlike Loucks et al. (2009) and Heath et al. (2011, their Figure 7), we observed no distinct pore types in organic phases. Energy-dispersive X-ray spectroscopic (EDS) chemical analysis was not done on these samples, however based on XRD analysis the clay matrix is probably mostly illite-smectite mixed layered clays. Figure 2(b) shows the range of observed pore types in the imaged Haynesville samples. These are similar in morphology to the slit pores (Type I), crescent-shaped pores in clay matrix (Type II), and pores adjacent to clastic grains in so-called compaction- or strain-shadows (Type III) described by Desbois et al. (2009) in tertiary boom clay (Belgium) and by Heath et al. (2011) in continental and marine mudstones from a variety of depositional environments and geologic ages (USA).

Slit pores are elongate and roughly perpendicular to the deposition direction (up in the photos in Figure 2) and a good example occurs just above the label in Figure 2(b). So-called Type II pores are crescent-shaped pores in folded clay fabrics, and are found throughout the clay matrix [surrounding the label in Figure 2(b)]. Type III pores are dominantly found in the compaction or strain shadows circumventing larger clastic quartz and feldspar grains and are generally triangular in cross section. Good examples are located adjacent to the centrally located labelled quartz grain in Figure 2(b). Many pore types are in fact hybrids of these three distinct morphologies, as seem to populate the sample imaged in Figure 2(c). In addition, pore types may originate from diagenetic reactions. The middle cluster of pores in Figure 2(d) may be interpreted as resulting from replacement of the illite-smectite matrix and is probably chlorite and associated calcite in-fill [light grey phase in Figure 2(d)]. The authors have observed similar chlorite 'rosette' morphologies in other mudstones that have been verified compositionally by EDS.

3.3 Pore network properties and tortuosity

Total porosity of the three-dimensional reconstruction of pore volumes in Figure 4 was calculated by voxel count to be 7.5%, representing a pore volume of 11.4 cubic microns. Ignoring pore voxels that touch the exterior of the imaged domain, this includes 97.8% disconnected pore voxels (most just a few voxels in size) and 2.15% connected voxels. Analysis of medial axes of connected pore voxels (i.e., the skeleton of connected pores calculated using the 3DMA-Rock software package developed by Lindquist, 1999) shown in Figure 5, discerns between pore bodies and pore throats. Open regions not containing medial axis voxels [the clear regions in Figure 5(a) and Figure 5(b)] are generally occupied by detrital grains of quartz or plagioclase. There appears to be near-linear regions of connected pores, or regions with dense distributions of medial axis voxels, running from the lower left to upper right region of Figure 5(a), which is suggestive of localised pathways of fluid migration. A total of 9,546 pores are defined in the imaged domain, including 8,674 pores within the interior of the imaged region, and 872 that touch the region boundaries.

The correlation between pore body size and topology is investigated through use of joint and marginal relative frequency histograms of pore body volume and coordination number [Figure 5(c)]. The pore body volumes exhibit a log10 normal distribution (top marginal histogram), apparently a typical distribution for pores in mudstones (Heath et al., 2011). The coordination number (i.e., number of connected, neighbouring pores) with the highest relative frequency is 2 (see the side marginal histogram), which coincides with the peak of the pore body volume distribution. Thus, the most frequently occurring pore body size has a coordination number of 2. This may represent the touching of slit-shaped Type I or triangular shaped Type II and Type III pores at their margins or tips. The up-and-to-the-right pattern within the joint histogram may reflect a scaling relationship between pore body size and coordination number. The second most frequent coordination number is zero, which corresponds with a range of pore body sizes, due to the occurrence of disconnected pores of a variety of sizes (at FIB-SEM resolution). The smallest imaged pores have coordination numbers of zero and 1, with 1 being the more frequent coordination number – showing that many small pores are part of connected networks.

The medial axes can be used to determine lengths of connected pores across the imaged domain and so be used to estimate tortuosity of possible flow paths. Figure 6(a), Figure 6(b), and Figure 6(c) depict calculated shortest paths using the 3DMA software and the medial axes voxels shown in Figure 5(a) and Figure 5(b). The x-pathways were chosen from left to right as shown, y-pathways were chosen from top to bottom as shown, and z-pathways were chosen from front to back as shown. In all cases many initial dendritic paths neck down to a single flow path as one proceeds through the imaged volume. Tortuosity is calculated by dividing the total distance between medial axis voxels on opposing faces by the Euclidian distance between the same voxels (Lindquist et al., 2005) and have been calculated for both the shortest paths shown in Figure 6(a) to Figure 6(c) and all connected paths (e.g., there are ~9 million connected paths in the y-direction). Binned probability histograms of tortuosity values in the x-, y-, and z-direction are shown in Figure 6(d), Figure 6(e), and Figure 6(f) respectively. In the x-direction, mean values include 2.1 for shortest paths and 2.2 for all paths with a range from ~1.5 to ~4.5. Similar values are obtained for the y- and z-directions (~2 for the y-direction and ~1.7 for the z-direction) which shows a surprising lack of anisotropy in the distributions of connected pathways.

3.4 Single phase fluid flow and permeability in two pore network types

The transition from vicinal (or surface-bound) water to bulk water properties probably occurs in pores of ~2–3 nm in size (Dewhurst et al., 1999) so that water in FIB/SEM-resolved pores likely behaves as bulk water. This suggests that we could apply a Stokes type of flow modelling to estimate flow properties of the imaged volumes. It is debatable whether the small volumes investigated in this section constitute a REV, but this is beyond the scope of this paper, requiring much more detailed characterisation of heterogeneity at all scales of the mudstone samples than is attempted here. Large portions of connected pores from the volume shown in Figure 4 can be isolated as networks and further examined for flow properties. Using a floodfill algorithm in *ScanIP*^{TM}, two regions of discrete connectivity (i.e., are separate connected networks

isolated from remaining pores) have been selected from the same initial volume and correspond to one network of Type II/Type III pores in between clastic grains [Figure 7(a) and Figure7(b)] and another corresponding to Type I or slit-like pores [Figure 7(c) and Figure 7(d)].

Figure 8 CFD simulation of fluid flow through the connected network of Figure 7(a) and Figure 7(b) (see online version for colours)

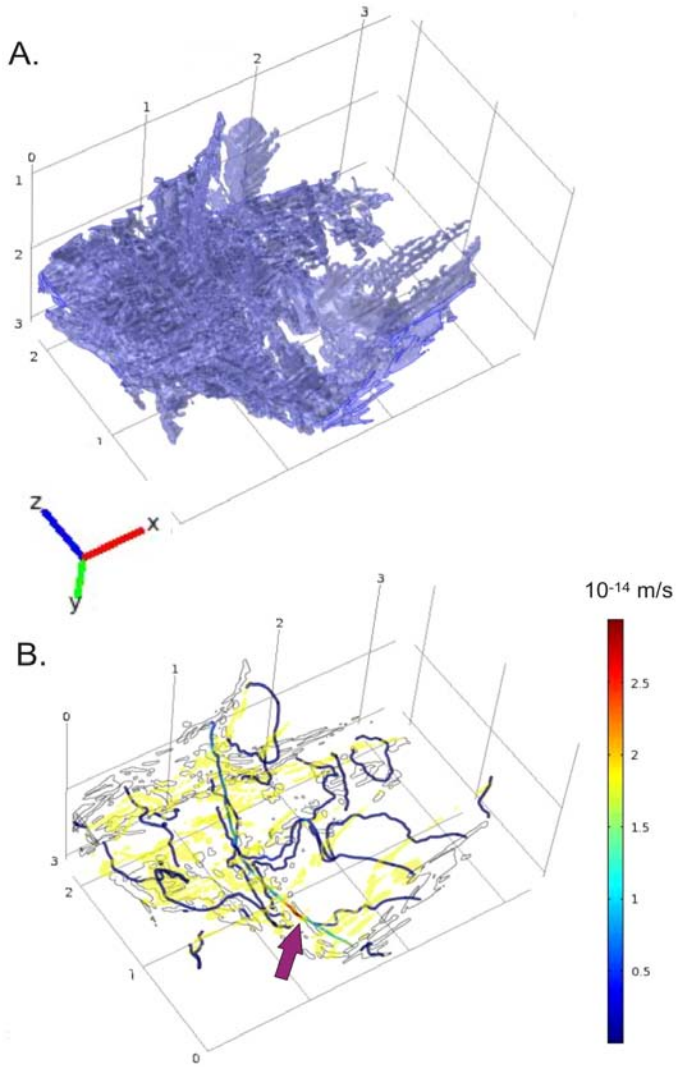

Notes: Units on axes of plots correspond to 10^{-6} metres (microns).
(a) Shows actual volume mesh and (b) shows streamlines through the volume. Yellow areas are cross sectional slices through the pore network. Colours of streamlines correspond to velocities, so the blue streamlines mostly correspond to dead-end pores while the rainbow-coloured streamline, delineated by the red arrow and corresponding to a portion of the shortest path in Figure 6(c), would be the dominant flow path.

Figure 9 CFD simulation of fluid flow through the 'slit'-pore network of Figure 7(c) and Figure 7(d) (see online version for colours)

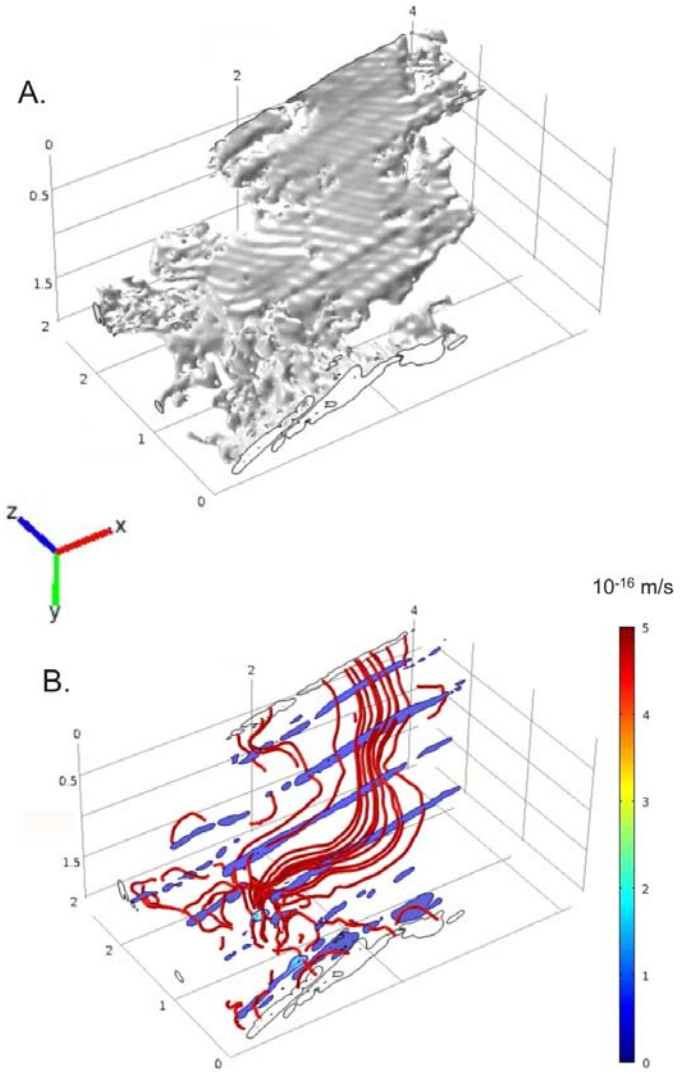

Notes: (a) shows the actual volume while (b) shows streamlines. Unlike the case in Figure 8, there is little dead-end volume indicated by the relatively uniform streamline velocities and the associated colours. Units on axes correspond to 10^{-6} metres (microns). Pore cross sectional areas are shown in blue. Flow direction is from bottom to top.

Figure 7(a) depicts a network of many small Type II and III pores, corresponding to an overall pore volume of 8.4 cubic microns. Figure 7(b) shows an image slice and cross section for that slice through the network of pores. The mesh generating algorithm of *ScanIP*^{TM} was used to generate a finite element mesh of this pore network consisting of ~35 million nodes [Figure 8(a)] to the software package *COMSOL Multiphysics*^{TM} for CFDs simulation. The fluid dynamics module in *COMSOLMultiphysics*^{TM} allows for

solution of the Navier-Stokes equations for modelling incompressible laminar flows in arbitrary geometries, and was ideal for obtaining estimates of permeability, as described in the *Methods* section. A small flux of 1.3×10^{-30} m^3/s was imposed across the simulated pore network with a small pressure gradient imposed at boundaries, which along with fluid properties and cross sectional area and using Darcy's Law [equation (1)] yields a permeability of 2.7 nanodarcys (equal to 2.6×10^{-21} m^2). Streamlines resulting from the simulation are shown in Figure 8(b). It is notable that only one streamline shows a velocity of any magnitude, labelled by the red arrow in Figure 8(b). The remaining streamlines have negligible flow velocities and thus can be considered as 'dead-end' pores. The former, 'fast' streamline corresponds to a portion of the shortest-path plotted in Figure 6(c).

A network consisting of two micron-sized Type I slit pores connected by a narrow pore throat is displayed in Figure 7(c), with Figure 7D showing a corresponding image slice and cross section. This network is smaller, with pore volume of only 0.9 cubic microns. A finite element mesh consisting of 580,000 nodes was used in a CFD simulation of incompressible laminar flow [Figure 9(a)]. A small steady-state flux of 2.8×10^{-30} m^3/s was imposed across the mesh with constant pressure boundary conditions and corresponds to a calculated permeability of 11 nanodarcys (equal to 1.1×10^{-20} m^2). In contrast to the pore network modelled in Figure 8, the streamline velocities would indicate that most of the pore volume in the slit-pore network is swept by flow, with little dead-end volume.

3.5 A comparison of MICP-derived and FIB-SEM pore throat distributions

A number of studies use pore body and pore throat statistics determined from image data sets to compare with properties discerned from MICP, with mixed results (e.g., Meyer and Klobes, 1999). This in large part is due to the simple bundle of tubes models used to infer pore throat size from mercury intrusion data, and the so-called 'ink-bottle' effect wherein small pore throats act as threshold capillary barriers to larger pores (Diamond, 2000). The larger pores, posing no capillary pressure barrier, would not be counted in the mercury data compilation of pore throat sizes. Thus MICP data generally are thought to overpredict the smaller pore throat sizes in a distribution. There is also the possiblity that the large intrusion pressures used in MICP could cause partial pore collapse of unsaturated smaller pores during an MICP test.

MICP capillary pressure curves for two core samples, corresponding to the samples near those used in the image analysis portion of this study, are shown in Figure 10(a). There is an almost linear increase in capillary pressure with non-wetting phase (i.e., mercury) saturation, which would correspond to a steady distribution of decreasing pore sizes intruded by mercury, with no large threshold of pore sizes (this would result in a plateau of the capillary pressure curve, as often seen in larger pore-sized rocks like sandstones, Almon et al., 2008). Pore throat radii data, as a probability distribution, from both MICP data and image data are plotted in Figure 10(b). It is clear that the mercury data would predict a dominance of pore sizes between 1 nm and 5 nm, while the FIB-SEM data predict a larger mean throat size, and in fact fall off below 10 nm (this is due to resolution issues with voxel sizes of 7.14 nm). It thus appears that MICP and image data sets are interrogating very different sets of pores.

Figure 10 Comparison of porosimetry and imaging pore distributions and scaling relationships (see online version for colours)

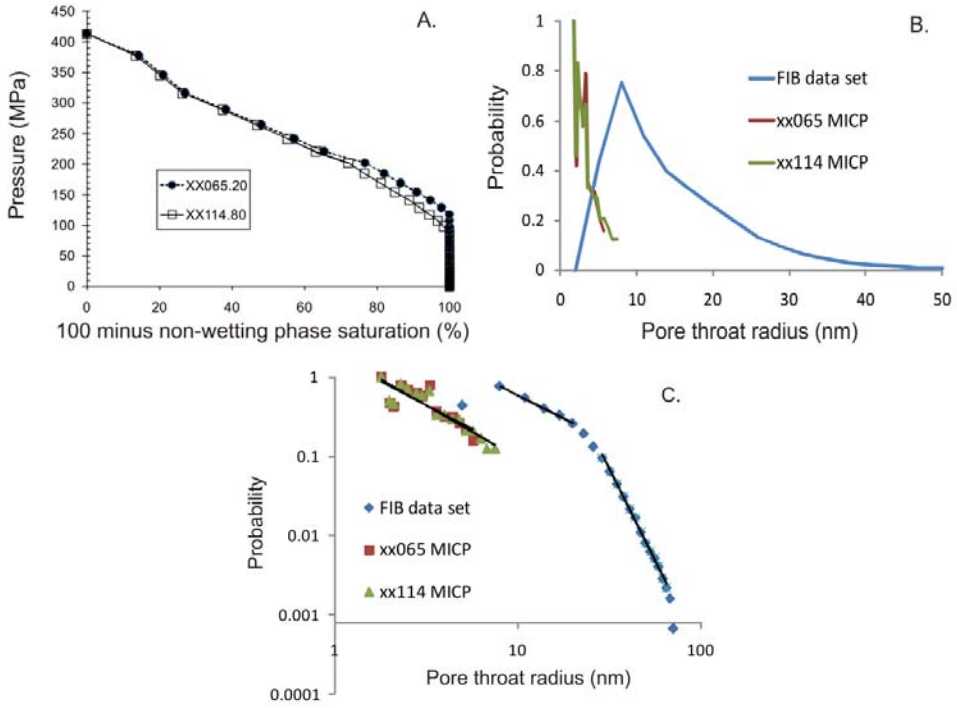

Notes: (a) Mercury intrusion capillary pressure (MICP) curves for two samples of the Haynesville formation taken near the depth of the sampled FIB-SEM volumes. The curves for two samples are essentially the same.

(b) Pore throat size distributions from MICP data compared to that determined from FIB-SEM reconstruction. The MICP data (which really are indicative of threshold dimensions) indicate a much smaller distribution of pore throats that are below the FIB-SEM resolution.

(c) Same as (b) but in log-log space. The FIB-SEM data set is suggestive of a bi-fractal relationship, with one power-law relation of smaller throats having the same slope (or fractal dimension) as the MICP data, and one of larger throats having a much larger slope, or fractal dimension, corresponding to throat radii larger than about 20 nm.

This is further shown in a log-log plot of the pore throat size distributions [Figure 10(c)] which indicate power-law scaling in pore throat sizes. Interestingly, the slopes of both sets of MICP data (–1.2 for the xx065 data set and –1.3 for the xx114 data set) are similar to a power-law slope (–1.2) for the smallest throats in the imaged data set distribution, between about 8 nm and 20 nm. For throat sizes larger than 20 nm, a different power-law scaling relationship appears to hold with slope equal to –4.6. There thus appears to be two sets of scaling relations corresponding to two sets of pores. One set of pores less than ~20 nm is observed by both MICP and image data sets, and one set of larger pores is observed only by the image data set. The former, which are barely resolvable as pores in the clay matrix of Figure 2, for example, dominate the capillary pressure relations of Figure 10(a). The latter form connected networks on the length scale of tens of microns

(our imaged volume) and may be responsible for the bulk measured absolute (single fluid phase) permeability.

4 Conclusions

From the above imaging and analysis, albeit from a limited small volume of 152 cubic microns, it appears that Haynesville Formation mudstones on the micron scale may behave as a dual porosity medium. Pores 10 nm in size or larger are resolvable using FIB-SEM methods (~7 nm pixel size), have mean volumes ~ 1×10^5 nm^3 connected to ~2 to 3 neighbours on average, and are bounded by throats with radii ~ 10 nm or more. Qualitatively these pores are slit shaped or form connected networks that bound adjacent clastic grains. Smaller pores 1–5 nm in size are indicated by MICP tests and likely reside in the interstices of clay mineral packets. Although mudstones in the Haynesville Formation are organic rich, we found few pores within or bound by masses of organic matter in the samples we examined (i.e., as seen by Loucks et al., 2009 or as shown by Heath et al., 2011, see their Figure 7).

Incompressible laminar modelling of flow in connected pore sub-volumes is used to calculate permeabilities for networks of larger pores in the range of 2 to 12 nanodarcys. While similar in magnitude to results of core-scale permeability tests using Haynesville mudstone samples (5–50 nanodarcys), any conclusion of similarity needs to be applied with caution given the small volume examined in this study. We make no claim as to what constitutes a REV in mudstones, but suggest that the methods detailed here could be used to discern REV's for different mudstone microfacies. It is nonetheless possible that single phase fluid flow is limited by pore throats similar in size and topology to that observed in the larger portion of the imaged pore throat distribution in Figure 10(c). The slit-like pores should be especially stress-sensitive and may be responsible for the order of magnitude decrease in measured core-plug permeability with factor of ~2 increase in confining pressure.

These pore types are to be distinguished from smaller pores, the largest of which are barely resolvable by FIB-SEM, with sizes at least as small as 1 nm determined by MICP. These pores are part of the clay matrix fabric itself, and would contain bound water with properties different than bulk water (Dewhurst et al., 1999). Such a dual-porosity model is similar to the conceptual model of Sanchez et al. (2008), as used by them in developing a mechanical constitutive model for partially saturated clays. FIB-SEM image data sets such as the ones presented here could be used to better constrain conceptual, pore scale, and continuum scale models for reactive transport, single and multiphase flow, and geomechanical response of shale gas formations.

Acknowledgements

The authors wish to thank Joe Michael and Michael Rye for help in acquiring the image slices and sample preparation. Brent Lindquist is thanked for providing the 3DMA-Rock software. The comments of three anonymous reviewers were of great benefit in preparing the manuscript and the authors thank them for their time and effort. The authors gratefully acknowledge funding from the US Department of Energy Office of Basic Energy Sciences, Division of Chemical Sciences, Geosciences, and Biosciences.

Sandia National Laboratories is a multi-program laboratory operated by Sandia Corporation, a wholly owned subsidiary of Lockheed Martin Corporation, for the US Department of Energy's National Nuclear Security Administration under contract DE-AC04-94AL85000.

References

Almon, W.R., Dawson, W.C., Botero-Duque, F., Goggin, L.R. and Yun, J.W. (2008) *Seal Analysis Workshop: Short Course Notes held at the Joint Annual Meeting of the Geological Society of America, Soil Science Society of America, American Society of Agronomy, Crop Science Society of America, and the Gulf Coast Association of Geological Studies with the Gulf Coast Section of SEPM*, 5–9 October, Houston, Texas.

De Winter, D.A.M., Schneijdenberg, C., Lebbink, M.N., Lich, B., Verkleij, A.J., Drury, M.R. and Humbel, B.M. (2009) 'Tomography of insulating biological and geological materials using focused ion beam (FIB) sectioning and low-kV BSE imaging', *Journal of Microscopy-Oxford*, Vol. 233, No. 3, pp.372–383.

Desbois, G., Urai, J.L. and Kukla, P.A. (2009) 'Morphology of the pore space in claystones – evidence from BIB/FIB ion beam sectioning and cryo-SEM obersvations', *e-Earth Discuss.*, Vol. 4, pp.1–19, doi:10.5194/eed-4-1-2009.

Desbois, G., Urai, J.L., Burkhardt, C., Drury, M.R., Hayles, M. and Humbel, B. (2008) 'Cryogenic vitrification and 3D serial sectioning using high resolution cryo-FIB SEM technology for brine-filled grain boundaries in halite: first results', *Geofluids*, Vol. 8, pp.60–72.

Dewhurst, D.N., Yang, Y. and Aplin, A. (1999) 'Permeability and fluid flow in natural mudstones', in Applin, A.C., Fleet, A.J. and Macquaker, J.H.S. (Eds.): *Muds and Mudstones: Physical and Fluid Flow Properties*, Vol. 158, pp.23–43, Geological Society of London Special Publications, Geological Society of London.

Diamond, S. (2000) 'Mercury porosimetry – an inappropriate method for the measurement of pore size distributions in cement-based materials', *Cement and Concrete Research*, Vol. 30, No. 10, pp.1517–1525.

Dobson, L.M. and Buffler, R.T. (1997) 'Seismic stratigraphy and geologic history of Jurassi Rocks, northeastern Gulf of Mexico', *A.A.P.G. Bulletin*, Vol. 81, No. 1, pp.100–120.

Ferreira, T.A. and Rasband, W. (2010) *The ImageJ User Guide – Version 1.43*, available at http://rsbweb.nih.gov/ij/docs/user-guide.pdf (accessed on March 2011).

Heath, J.E., Dewers, T.A., McPherson, B.J.O.L., Petrusak, R., Chidsey, T.C. Jr., Rinehart, A. and Mozley, P.S. (2011) 'Pore networks in continental and marine mudstones: characteristics and controls on sealing behavior', *Geosphere*, Vol. 7, No. 5, pp.429–454.

Holzer, L., Indutnyi, F., Gasser, P.H., Munch, B. and Wegmann, M. (2004) 'Three-dimensional analysis of porous BaTiO3 ceramics using FIB nanotomography', *Journal of Microscopy-Oxford*, Vol. 216, No. 1, pp.84–95.

Jones, S.C. (1997) 'A technique for faster pulse-decay permeability measurements in tight rocks', *Society of Petroleum Engineers Journal*, Vol. 12, No. 1, pp.19–26.

Lindquist, W.B. (1999) Report No. SUSB-AMS-99-20, Dept. Applied Math. & Stat., SUNY – Stony Brook.

Lindquist, W.B. and Venkatarangan, A. (1999) 'Investigating 3D geometry of porous media from high resolution images', *Physics and Chemistry of the Earth Part A-Solid Earth and Geodesy*, Vol. 24, No. 7, pp.593–599.

Lindquist, W.B., Lee, S.M., Oh., W., Venkatarangan, A.B., Shin, H. and Prodanovic, M. (2005) *3DMA-Rock: A Software Package for Automated Analysis of Rock Pore Structure in 3-D Computed Microtomography Images*, State University of New York at Stony Brook, http://www.ams.sunysb.edu/~lindquis/3dma/3dma_rock/3dma_rock.html (accessed on March 2011).

Loucks, R.G., Reed, R.M., Ruppel, S.C. and Jarvie, D.M. (2009) 'Morphology, genesis, and distribution of nanometer-scale pores in siliceous mudstones of the Mississippian Barnett Shale', *Journal of Sedimentary Research*, Vol. 79, pp.848–861.

Mancini, E.A., Epsman, M.L. and Stief, D.D. (1997) 'Characterization and evaluation of the Upper Jurassic Frisco City sandstone reservoir in southwestern Alabama utilizing Fullbore Formation MicroImager technology', *Gulf Coast Association of Geological Societies Transactions*, Vol. 47, pp.329–335.

Meijering, E. (2010) *TransformJ – A Java Package for Geometrical Image Transformation*, available at http://www.imagescience.org/meijering/software/transformj/ (accessed on March 2011).

Meyer, K. and Klobes, P. (1999) 'Comparison between different presentations of pore size distribution in porous materials', *Fresenius Journal of Analytical Chemistry*, Vol. 363, pp.174–178.

Rasband, W.S. (2010) *ImageJ*, National Institutes of Health, Bethesda, Maryland, USA, available at http://rsb.info.nih.gov/ij/ (accessed on March 2011).

Sanchez, M., Gens, A., Guimaraes, L. and Olivella, S. (2008) 'Implementation algorithm of a generalized plasticity model for swelling clays', *Computers and Geotechnics*, Vol. 35, No. 6, pp.860–871.

Shin, S., Lindquist, W.B., Sahagian, D.L. and Song, S-R. (2005) 'Analysis of the vesicular structure of basalts', *Computers and Geosciences*, Vol. 31, No. 4, pp.473–487.

Sigal, R.F. (2009) 'A methodology for blank and conformance corrections for high pressure mercury porosimetry', *Measurement Science and Technology*, Vol. 20, No. 4, doi: 10.1088/0957-0233/20/4/045108.

Srodon, J., Drits, V.A., McCarty, D.K., Hsieh, J.C.C. and Eberl, D.D. (2001) 'Quantitative X-ray diffraction analysis of clay-bearing rocks from random preparations', *Clays and Clay Minerals*, Vol. 49, pp.514–528.

Tolson, J.S., Copeland, C.W. and Bearden, B.L. (1983) 'Stratigraphic profiles of Jurassic strata in the western part of the Alabama Coastal Plain', *Geological Survey of Alabama Bulletin*, Vol. 122, p.425.

Tomutsa, L., Silin, D. and Radmilovic, V. (2007) 'Analysis of chalk petrophysical properties by means of submicron-scale pore imaging and modeling', *SPE Reservoir Evaluation and Engineering*, Vol. 10, No. 3, pp.285–293.

Yao, N. (2007) 'Introduction to the focused ion beam system', in Yao, N. (Ed.): *Focused Ion Beam Systems: Basics and Applications*, Cambridge University Press, Cambridge, UK.